EDGE ARTICLE

Check for updates

Tuning the photophysical properties of lanthanide(III)/zinc(II) 'encapsulated sandwich' metallacrowns emitting in the near-infrared range†

Svetlana V. Eliseeva, [ID] ‡*[a] Tu N. Nguyen, [ID] ‡§[b] Jeff W. Kampf,[b] Evan R. Trivedi, [ID] ¶[b] Vincent L. Pecoraro [ID] *[b] and Stéphane Petoud [ID] *[a]

A family of $Zn_{16}Ln(HA)_{16}$ metallacrowns (MCs; Ln = Yb^{III}, Er^{III}, and Nd^{III}; HA = picoline- ($picHA^{2-}$), pyrazine- ($pyzHA^{2-}$), and quinaldine- ($quinHA^{2-}$) hydroximates) with an 'encapsulated sandwich' structure possesses outstanding luminescence properties in the near-infrared (NIR) and suitability for cell imaging. Here, to decipher which parameters affect their functional and photophysical properties and how the nature of the hydroximate ligands can allow their fine tuning, we have completed this $Zn_{16}Ln(HA)_{16}$ family by synthesizing MCs with two new ligands, naphthyridine- ($napHA^{2-}$) and quinoxaline- ($quinoHA^{2-}$) hydroximates. $Zn_{16}Ln(napHA)_{16}$ and $Zn_{16}Ln(quinoHA)_{16}$ exhibit absorption bands extended into the visible range and efficiently sensitize the NIR emissions of Yb^{III}, Er^{III}, and Nd^{III} upon excitation up to 630 nm. The energies of the lowest singlet (S_1), triplet (T_1) and intra-ligand charge transfer (ILCT) states have been determined. Ln^{III}-centered total (Q_{Ln}^L) and intrinsic (Q_{Ln}^{Ln}) quantum yields, sensitization efficiencies (η_{sens}), observed (τ_{obs}) and radiative (τ_{rad}) luminescence lifetimes have been recorded and analyzed in the solid state and in CH_3OH and CD_3OD solutions for all $Zn_{16}Ln(HA)_{16}$. We found that, within the $Zn_{16}Ln(HA)_{16}$ family, τ_{rad} values are not constant for a particular Ln^{III}. The close in energy positions of T_1 and ILCT states in $Zn_{16}Ln(picHA)_{16}$ and $Zn_{16}Ln(quinHA)_{16}$ are preferred for the sensitization of Ln^{III} NIR emission and η_{sens} values reach 100% for Nd^{III}. Finally, the highest values of Q_{Ln}^L are observed for $Zn_{16}Ln(quinHA)_{16}$ in the solid state or in CD_3OD solutions. With these data at hand, we are now capable of creating MCs with desired properties suitable for NIR optical imaging.

Introduction

The numerous advantages of non-invasive near-infrared (NIR) optical imaging for biological applications[1–4] have stimulated significant advances in the creation of novel probes for cell, tissue and organ visualization. Among the different classes of NIR imaging probes,[5,6] Ln^{III}-based molecular compounds can offer complementary advantages,[7] in particular, sharp emission bands with defined positions, large energy difference between excitation and emission wavelengths, and high photostability. Apart from biological applications, the NIR emission arising from Ln^{III} complexes can be used in material sciences, telecommunications, light-emitting diodes, night vision displays, security inks, and solar energy conversion.[8,9] However, for the design of highly NIR-emitting Ln^{III} molecular compounds, several challenges have to be addressed.[10,11] The emission efficiency of Ln^{III} complexes is quantified by the following equation:

$$Q_{Ln}^L = \eta_{sens} \times Q_{Ln}^{Ln} = \eta_{sens} \times \frac{\tau_{obs}}{\tau_{rad}} \quad (1)$$

where Q_{Ln}^L is the total quantum yield obtained under ligand excitation, η_{sens} is the sensitization efficiency of the organic ligands taking into account the energy migration processes occurring both within the ligands and from the ligand to the Ln^{III} excited state, Q_{Ln}^{Ln} is the intrinsic quantum yield or quantum yield upon direct f–f excitation, which reflects the relative impact of radiative and non-radiative processes occurring around Ln^{III}, and τ_{rad} is the radiative lifetime or the luminescence lifetime in absence of non-radiative deactivation processes. In view of practical applications, the brightness of

a Ln^{III} compound is defined as $\varepsilon \times Q_{Ln}^{L}$, where ε is the molar absorption coefficient.

The first requirement to obtain high Q_{Ln}^{L} is to optimize energy migration processes, in particular η_{sens}. This parameter is mainly dependent on the nature of the organic ligands and the relative positions of their electronic levels (lowest singlet S_1, triplet T_1 or charge transfer (CT) states) with respect to the accepting levels of Ln^{III}.[10,11] In this respect, several phenomenological rules have been developed for visible-emitting Ln^{III} complexes.[12–15] On the other hand, no clear correlations have been established for coordination compounds incorporating NIR-emitting Ln^{III} while the choice of chromophores is much wider and includes molecules absorbing light in the visible and the NIR ranges.[16–20] A second important challenge is to minimize sources of non-radiative deactivation mechanisms (overtones of high-energy vibrations, CT states, back energy transfer processes) that decrease observed luminescence lifetimes and, in turn, the corresponding intrinsic quantum yields. Avoiding sources of non-radiative deactivation taking places through overtones of not only O–H and N–H, but also C–H vibrations that are widely present in complexes formed with organic ligands, is of particular importance for NIR-emitting Ln^{III} because of the small energy gaps between the emitting and the receiving states. The most widely used strategy to overcome this limitation is by halogenation[18,19,21–23] or by deuteration[24–26] of the organic ligands. Another approach to minimize non-radiative deactivations is to create a protective hydrophobic environment around the Ln^{III} ion as in the case of complexes formed with imidodiphosphonate ligands.[27,28] In addition, according to eqn (1), one more parameter that can be tuned and that lead to the enhancement of Q_{Ln}^{L} is the radiative lifetime. The validity of this approach has been demonstrated in several studies.[26,29–31]

Recently, our group has pioneered a new approach toward the design of NIR-emitting Ln^{III} complexes that take advantage of metallacrown (MC) scaffolds.[32–38] MCs are a class of inorganic macrocycles forming repeating [metal–N–O] subunits.[39] These MC complexes possess oxygen atoms oriented toward the center of the ring allowing an efficient pre-organization for cation encapsulation in a manner similar to classical organic crown ethers.

We created a family of NIR-emitting $Zn_{16}Ln(HA)_{16}$ MCs assembled using picoline- ($picHA^{2-}$),[33] pyrazine- ($pyzHA^{2-}$),[37] and quinaldine-($quinHA^{2-}$)[32] hydroximate ligands (Fig. 1) and demonstrated their promising applications for NIR cell imaging.[37,38] The unique 'encapsulated sandwich' structure of this family of MCs not only allows for highly efficient sensitization of the characteristic emissions from Yb^{III}, Nd^{III} and Er^{III} but also locates the luminescent Ln^{III} ion at a relatively long distance (~7 Å) from C–H oscillators present on the organic ligands, thereby minimizing the effect of non-radiative deactivation. We have demonstrated that the nature of the hydroxamate ligand affects not only the luminescence but also the functional properties, such as the water solubility obtained for MCs formed with the $pyzHA^{2-}$ chromophoric building-block. However, the absorption maxima of all previously reported $Zn_{16}Ln(HA)_{16}$ MCs have remained in the UV range. An excitation light in the UV domain is detrimental for practical applications such as
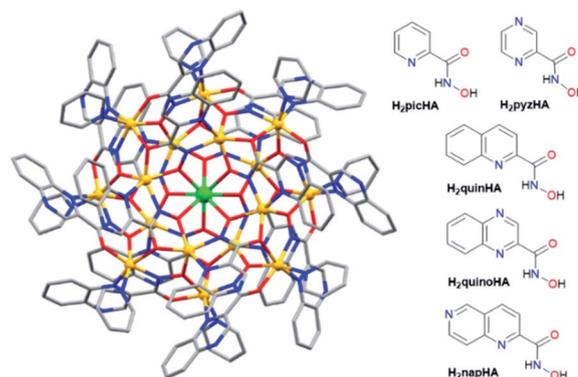

Fig. 1 (Left) Molecular structure of the $Zn_{16}Yb(quinoHA)_{16}$ MC obtained by single crystal X-ray diffraction. Color code: green, Yb; yellow, Zn; red, O; blue, N; grey, C. H atoms and solvents have been omitted for clarity. (right) Structures of the hydroxamic acids used to assemble 'encapsulated sandwich' MCs.

biological optical imaging due to strong interaction with biological tissues or fluids, resulting in their disturbance or damage.

Therefore, in this work, we expand the $Zn_{16}Ln(HA)_{16}$ family by creating MCs with two new ligands, naphthyridine- ($napHA^{2-}$) and quinoxaline- ($quinoHA^{2-}$) hydroximate (Fig. 1) following the specific goal of shifting the absorption wavelength further into the visible region. In addition, this comprehensive study that includes $Zn_{16}Ln(HA)_{16}$ MCs with a full range of substitution patterns addresses the general goal of bringing a rationalization for the smart tuning of the functional and photophysical properties, with a specific focus on NIR emission, on the basis of the nature of the hydroximate ligand. Synthesis and characterization of new $Zn_{16}Ln(napHA)_{16}$ and $Zn_{16}Ln(quinoHA)_{16}$ MCs formed with several lanthanide cations (Ln = Yb^{III}, Er^{III}, Nd^{III}, Gd^{III}) and Y^{III}, including the structural analysis of $Zn_{16}Nd(quinoHA)_{16}$ and $Zn_{16}Yb(quinoHA)_{16}$, are reported. Absorption, excitation, and emission spectra, total and intrinsic quantum yields, sensitization efficiencies, observed and radiative lifetimes were acquired and extensively analyzed herein for the NIR-emitting $Zn_{16}Ln(napHA)_{16}$ and $Zn_{16}Ln(quinoHA)_{16}$ (Ln = Yb^{III}, Er^{III}, Nd^{III}) in the solid state and in CH_3OH and CD_3OD solutions. Moreover, we completed the detailed photophysical studies for $Zn_{16}Ln(picHA)_{16}$, $Zn_{16}Ln(pyzHA)_{16}$ and $Zn_{16}Ln(quinHA)_{16}$ by recording Q_{Ln}^{Ln} for Nd^{III} and Er^{III} analogues or τ_{rad} for Yb^{III}. Our approach allows the quantification of all relevant parameters from eqn (1), in particular τ_{obs}, τ_{rad}, η_{sens} and Q_{Ln}^{Ln}, and their impact on the total quantum yield Q_{Ln}^{L} within the series of $Zn_{16}Ln(HA)_{16}$ MCs created with the different hydroximate ligands.

Experimental

All syntheses were performed under aerobic conditions using chemicals and solvents as received unless otherwise stated. ESI-MS spectra were collected with a Micromass LCT time-of-flight electrospray mass spectrometer in a negative ion mode at a cone voltage of −40 V on samples dissolved in CH_3OH. Samples were injected via a syringe pump. Data were processed with the

program MassLynx 4.0. Elemental analyses were performed by Atlantic Microlabs Inc.

Synthesis of quinoxalinehydroxamic acid (H$_2$quinoHA)

In a three-neck flask, 2-quinoxalinecarboxylic acid (3.1 g, 18.0 mmol) was added into a solution of N-methylmorpholine (2.4 mL, 21.8 mmol) in dichloromethane (50.0 mL). The mixture was stirred under N$_2$ for 15 minutes and cooled down to 0 °C. Ethylchloroformate (2.0 mL, 21.0 mmol) was added dropwise under stirring. The mixture was stirred for an additional 1 hour and filtered to obtain a brown solution. Meanwhile, a fresh hydroxylamine solution was prepared by reacting hydroxylamine hydrochloride (1.9 g, 27.0 mmol) with potassium hydroxide at 85% (1.8 g, 27.0 mmol) in methanol (16.0 mL) at 0 °C. The solution was stirred for 10 minutes, filtered, and the filtrate obtained was added dropwise into the brown solution while stirring at 0 °C. The reaction mixture was stirred for 2 hours, filtered, and the filtrate was left for slow evaporation to induce the precipitation of a white solid. The solid was recrystallized in hot water, collected by filtration, washed with a copious amount of water, and dried under vacuum to yield the pure powder of H$_2$quinoHA. Yield ~26% (0.90 g), ESI-MS, calc. for [M − H$^+$], C$_9$H$_6$N$_3$O$_2$, 188.05; found 188.0. ^{1}H NMR (400 MHz, DMSO-d_6) δ ppm 11.78 (s, 1H), 9.40 (s, 1H), 9.37 (s, 1H), 8.20–8.15 (m, 2H), 8.00–7.95 (m, 2H). ^{13}C NMR (400 MHz, DMSO-d_6) δ ppm 161.0, 144.7, 143.6, 142.8, 139.8, 131.7, 131.2, 129.4, 129.1. Elem. anal., calc. (found) for (C$_9$H$_7$N$_3$O$_2$), C: 57.14 (57.42), H: 3.73 (3.85), N: 22.21 (22.06).

Synthesis of naphthyridinehydroxamic acid (H$_2$napHA)

H$_2$napHA was synthesized in two steps.

Step 1: to a stirred solution of 1,6-naphthyridine-2-carboxylic acid (0.20 g, 1.1 mmol) in 20.0 mL of CH$_3$OH, 1.0 mL of H$_2$SO$_4$ was added dropwise. The solution was then refluxed for 6 hours. After cooling down to room temperature, the solution was neutralized by a CH$_3$OH solution of NaOH until the formation of a solid which was filtered, washed with H$_2$O, and dried under vacuum to obtain methyl naphthyridine-2-carboxylate. Yield: ~56% (0.12 g). ^{1}H NMR (400 MHz, CDCl$_3$) δ ppm 9.37 (s, 1H), 8.84 (d, 1H), 8.46 (d, 1H), 8.31 (d, 1H), 8.10 (d, 1H), 4.09 (s, 3H).

Step 2: without further purification, 0.095 g (0.50 mmol) of methyl naphthyridine-2-carboxylate was added to a 15.0 mL solution of CH$_3$OH containing 0.40 g of hydroxylamine hydrochloride. An amount of 0.32 g of NaOH was added and the resulting solution was stirred at room temperature overnight. CH$_3$OH was then removed under vacuum to give a solid, which was washed by a dilute HCl solution to give pure H$_2$napHA. Yield: ~53% (0.050 g). ESI-MS, calc. for [M − H$^+$], C$_9$H$_6$N$_3$O$_2$, 188.05; found 188.0. ^{1}H NMR (400 MHz, DMSO-d_6) δ ppm 11.71 (s, 1H), 9.50 (s, 1H), 9.32 (s, 1H), 8.82 (d, 1H), 8.76 (d, 1H), 8.21 (d, 1H), 7.95 (d, 1H). Elem. anal., calc. (found) for (C$_9$H$_7$N$_3$O$_2$), C: 57.14 (57.26), H: 3.73 (3.70), N: 22.21 (22.10).

Synthesis of Zn$_{16}$Ln(quinoHA)$_{16}$ and Zn$_{16}$Ln(napHA)$_{16}$ (Ln = Nd^{III}, Gd^{III}, Er^{III}, Yb^{III}) and the Y^{III} analogues

A general synthesis for these compounds is described below for the Zn$_{16}$Nd(quinoHA)$_{16}$ complex. Complexes with Y^{III}, other Ln^{III} and napHA^{2-} were prepared by substituting the appropriate metal ion for Nd^{III} and hydroxamic acid for H$_2$quinoHA. Deuterated pyridine (py-d_5) was used in the syntheses of the Y^{III} analogues.

[Zn$_{16}$Nd(quinoHA)$_{16}$(py)$_8$](OTf)$_3$ (Zn$_{16}$Nd(quinoHA)$_{16}$). H$_2$quinoHA (0.060 g, 0.32 mmol) was added to a solution containing 1.0 mL pyridine, 5.0 mL DMF, and 5.0 mL H$_2$O. The solution was stirred for 5 minutes in order to completely dissolve the solid. Zinc triflate (0.12 g, 0.32 mmol) and neodymium triflate (0.024 g, 0.040 mmol) were added and the orange solution was stirred at 80 °C for 2 hours. The solution was then cooled down to room temperature, and filtered. The filtrate was layered with H$_2$O to give red–brown crystals after three days. The crystals were collected by filtration, washed with H$_2$O, and dried in air. Yield ~28% (31 mg). ESI-MS (CH$_3$OH), calc. for [M]$^{3+}$, Zn$_{16}$NdC$_{144}$H$_{80}$N$_{48}$O$_{32}$, 1392.79; found 1393.0. Elem. anal., calc. (found) for (Zn$_{16}$NdC$_{187}$H$_{120}$N$_{56}$O$_{41}$F$_9$S$_3$)(H$_2$O)$_{12}$, C: 40.98 (40.67), H: 2.65 (2.38), N: 14.31 (14.24).

[Zn$_{16}$Gd(quinoHA)$_{16}$(py)$_8$](OTf)$_3$ (Zn$_{16}$Gd(quinoHA)$_{16}$). Yield ~35% (38 mg). ESI-MS (CH$_3$OH), calc. for [M]$^{3+}$, Zn$_{16}$GdC$_{144}$H$_{80}$N$_{48}$O$_{32}$, 1398.13; found 1396.8. Elem. anal., calc. (found) for (Zn$_{16}$GdC$_{187}$H$_{120}$N$_{56}$O$_{41}$F$_9$S$_3$)(H$_2$O)$_{12}$, C: 40.88 (40.68), H: 2.64 (2.26), N: 14.28 (14.13).

[Zn$_{16}$Er(quinoHA)$_{16}$(py)$_8$](OTf)$_3$ (Zn$_{16}$Er(quinoHA)$_{16}$). Yield ~24% (26 mg). ESI-MS (CH$_3$OH), calc. for [M]$^{3+}$, Zn$_{16}$ErC$_{144}$H$_{80}$N$_{48}$O$_{32}$, 1400.79; found 1400.3. Elem. anal., calc. (found) for (Zn$_{16}$ErC$_{187}$H$_{120}$N$_{56}$O$_{41}$F$_9$S$_3$)(H$_2$O)$_{12}$, C: 40.81 (40.85), H: 2.64 (2.43), N: 14.25 (14.38).

[Zn$_{16}$Yb(quinoHA)$_{16}$(py)$_8$](OTf)$_3$ (Zn$_{16}$Yb(quinoHA)$_{16}$). Yield ~23% (25 mg). ESI-MS (CH$_3$OH), calc. for [M]$^{3+}$, Zn$_{16}$YbC$_{144}$H$_{80}$N$_{48}$O$_{32}$, 1403.46; found 1403.4. Elem. anal., calc. (found) for (Zn$_{16}$YbC$_{187}$H$_{120}$N$_{56}$O$_{41}$F$_9$S$_3$)(H$_2$O)$_{12}$, C: 40.76 (40.90), H: 2.63 (2.39), N: 14.24 (14.26).

[Zn$_{16}$Y(quinoHA)$_{16}$(py-d_5)$_8$](OTf)$_3$ (Zn$_{16}$Y(quinoHA)$_{16}$). ESI-MS (CH$_3$OH), calc. for [M]$^{3+}$, Zn$_{16}$YbC$_{144}$H$_{80}$N$_{48}$O$_{32}$, 1375.12; found 1373.4.

[Zn$_{16}$Nd(napHA)$_{16}$(py)$_8$](OTf)$_3$ (Zn$_{16}$Nd(napHA)$_{16}$). Yield ~27% (30 mg). ESI-MS (CH$_3$OH), calc. for [M]$^{3+}$ Zn$_{16}$NdC$_{144}$H$_{80}$N$_{48}$O$_{32}$, 1392.79; found 1393.0. Elem. anal., calc. (found) for (Zn$_{16}$NdC$_{187}$H$_{120}$N$_{56}$O$_{41}$F$_9$S$_3$)(H$_2$O)$_{12}$, C: 40.98 (40.70), H: 2.65 (2.52), N: 14.31 (14.10).

[Zn$_{16}$Gd(napHA)$_{16}$(py)$_8$](OTf)$_3$ (Zn$_{16}$Gd(napHA)$_{16}$). Yield ~32% (35 mg). ESI-MS (CH$_3$OH), calc. for [M]$^{3+}$, Zn$_{16}$GdC$_{144}$H$_{80}$N$_{48}$O$_{32}$, 1398.13; found 1397.7. Elem. anal., calc. (found) for (Zn$_{16}$GdC$_{187}$H$_{120}$N$_{56}$O$_{41}$F$_9$S$_3$)(H$_2$O)$_{12}$, C: 40.88 (40.67), H: 2.64 (2.65), N: 14.28 (14.30).

[Zn$_{16}$Er(napHA)$_{16}$(py)$_8$](OTf)$_3$ (Zn$_{16}$Er(napHA)$_{16}$). Yield ~24% (26 mg). ESI-MS (CH$_3$OH), calc. for [M]$^{3+}$, Zn$_{16}$ErC$_{144}$H$_{80}$N$_{48}$O$_{32}$, 1400.79; found 1401.1. Elem. anal., calc. (found) for (Zn$_{16}$ErC$_{187}$H$_{120}$N$_{56}$O$_{41}$F$_9$S$_3$)(H$_2$O)$_{12}$, C: 40.81 (40.71), H: 2.64 (2.66), N: 14.25 (14.22).

[Zn$_{16}$Yb(napHA)$_{16}$(py)$_8$](OTf)$_3$ (Zn$_{16}$Yb(napHA)$_{16}$). Yield ~27% (30 mg). ESI-MS (CH$_3$OH), calc. for [M]$^{3+}$, Zn$_{16}$YbC$_{144}$H$_{80}$N$_{48}$O$_{32}$, 1403.46; found 1403.0. Elem. anal., calc. (found) for (Zn$_{16}$YbC$_{187}$H$_{120}$N$_{56}$O$_{41}$F$_9$S$_3$)(H$_2$O)$_{12}$, C: 40.76 (40.60), H: 2.63 (2.71), N: 14.24 (14.11).

$[Zn_{16}Y(napHA)_{16}(py-d_5)_8](OTf)_3$ $(Zn_{16}Y(napHA)_{16})$. ESI-MS (CH_3OH), calc. for $[M]^{3+}$, $Zn_{16}YC_{144}H_{80}N_{48}O_{32}$, 1375.12; found 1375.1.

X-ray crystallography

Orange blocks of $Zn_{16}Nd(quinoHA)_{16}$ and $Zn_{16}Yb(quinoHA)_{16}$ were grown from a dimethylformamide/water solution of the compound at 22 °C. A crystal of dimensions 0.20 × 0.19 × 0.14 mm for the former, and 0.12 × 0.11 × 0.08 mm for the latter, was mounted on a Rigaku AFC10K Saturn 944+ CCD-based X-ray diffractometer equipped with a low temperature sample conditioning device and a Micromax-007HF Cu-target micro-focus rotating anode (λ = 1.54187 A) operated at 1.2 kW power (40 kV, 30 mA). The X-ray intensities were measured at 85(1) K with the detector placed at a distance 42.00 mm from the crystal.

For $Zn_{16}Nd(quinoHA)_{16}$, a total of 4125 images were collected with an oscillation width of 1.0° in ω. Exposure times were 5 s and 25 s for the low- and high-angle images respectively. Rigaku d*trek images were exported to CrysAlisPro for the processing of the collected data and corrected for absorption. The integration of the experimental data yielded a total of 472 686 reflections to a maximum 2θ value of 148.15° of which 12 397 were independent and 11 558 were greater than $2\sigma(I)$. The final cell constants (Table S1†) were based on the xyz centroids of 129 624 reflections described above $10\sigma(I)$. The analysis of the data showed a negligible intensity decay during data collection. The structure was solved and refined with the Bruker SHELXTL (version 2014/6) software package[40] and using the space group $P4/ncc$ with Z = 4 for the formula $C_{187}H_{120}N_{62}O_{57.5}F_9S_3Zn_{16}Nd$. All non-hydrogen atoms were refined anisotropically with the hydrogen atoms placed in idealized positions. Full matrix least-squares refinements based on F^2 converged at R_1 = 0.0550 and wR_2 = 0.1902 [based on $I > 2\sigma(I)$], R_1 = 0.0572 and wR_2 = 0.1943 for all data. The SQUEEZE subroutine of the PLATON program suite[41] was used to address highly disordered solvent and two triflate anions present in the structure. Additional details are presented in Table S1.†

For $Zn_{16}Yb(quinoHA)_{16}$, a total of 2289 images were collected with an oscillation width of 1.0° in ω. The exposure times were 5 s and 25 s for the low- and high-angle images. The integration of the experimental data yielded a total of 386 106 reflections to a maximum 2θ value of 136.49° of which 11 168 were independent and 9078 were greater than $2\sigma(I)$. The final cell constants (Table S2†) were based on the xyz centroid 143 200 reflections above $10\sigma(I)$. Analysis of these data showed negligible intensity decay during data collection. They were processed with CrystalClear 2.0 and corrected for their absorption. The structure was solved and refined with the Bruker SHELXTL (version 2014/6) software package,[40] using the space group $P4/ncc$ with Z = 4 for the formula $C_{187}H_{124.5}N_{56}O_{47}F_9S_3Zn_{16}Yb$. All non-hydrogen atoms were refined anisotropically with the hydrogen atoms placed on idealized positions. Full matrix least-squares refinement based on F^2 converged at R_1 = 0.0687 and wR_2 = 0.2087 [based on $I > 2\sigma(I)$], R_1 = 0.0768 and wR_2 = 0.2193 for all data. The SQUEEZE subroutine of the PLATON program suite[41] was used to address highly disordered solvent and two triflate anions present in the structure. Additional details are presented in Table S2.†

Photophysical measurements

Data were collected on samples in the solid state or on freshly prepared solutions placed in 2.4 mm i.d. quartz capillaries or quartz Suprasil cells. Absorption spectra were acquired on a Varian Cary 100Bio or a Jasco V670 spectrophotometer in absorbance mode. Steady-state emission and excitation spectra were measured on a Horiba-Jobin-Yvon Fluorolog 3 spectrofluorimeter equipped with either a visible photomultiplier tube (PMT) (220–800 nm, R928P; Hamamatsu), a NIR solid-state InGaAs detector cooled to 77 K (800–1600 nm, DSS-IGA020L; ElectroOptical Systems, Inc., USA), or a NIR PMT (950–1650 nm, H10330-75; Hamamatsu). Phosphorescence spectra of Gd^{III} MCs were acquired in the solid state at 77 K on a Fluorolog 3 spectrofluorimeter in a time-resolved mode. All spectra were corrected for the instrumental functions. Luminescence lifetimes were determined under excitation at 355 nm provided by a Nd:YAG laser (YG 980; Quantel). Signals in the NIR range were detected by the NIR H10330-75 PMT connected to an iHR320 monochromator (Horiba Scientific). The output signals generated from the detectors were fed into a 500 MHz bandpass digital oscilloscope (TDS 754C; Tektronix) and transferred to a PC for data processing with the Origin 8® software. Luminescence lifetimes are averages of three or more independent measurements. Quantum yields were determined with a Fluorolog 3 spectrofluorimeter based on the absolute method using an integration sphere (GMP SA). Each sample was measured several times. Experimental error for the determination of quantum yields is estimated as ~10%.

Results

Synthesis

$Zn_{16}Ln(napHA)_{16}$ and $Zn_{16}Ln(quinoHA)_{16}$ were prepared using a modified synthetic procedure in respect to the one reported previously for $Zn_{16}Ln(HA)_{16}$ (HA = $picHA^{2-}$, $pyzHA^{2-}$, $quinHA^{2-}$).[32,33,37] The self-assembly reaction between H_2napHA or $H_2quinoHA$, Zn^{II} and Ln^{III} triflates was performed in a DMF/H_2O/pyridine solution. The use of an excess of Ln^{III} triflates (molar ratio $Zn(OTf)_2$: $Ln(OTf)_3$ 8 : 1) ensures the formation of pure products. All reactions can be performed at room temperature but significantly higher yields were obtained when the reaction mixtures were heated to 80 °C. All synthesized MCs were systematically characterized by ESI mass-spectrometry (ESI†) and elemental analysis. According to the elemental analysis, the general composition of the MCs can be presented as follows $[Zn_{16}Ln(HA)_{16}(py)_8](OTf)_3(H_2O)_{12}$, in which each MC molecule contains 1 Ln^{III}, 16 Zn^{II}, 16 naphthyridine- ($napHA^{2-}$) or quinoxaline- ($quinoHA^{2-}$) hydroximates, 8 pyridine molecules coordinated to Zn^{II} ions, three triflate anions as counterions and 12 water molecules. An ESI-MS analysis has been performed in a positive mode, so only $[Zn_{16}Ln(HA)_{16}]^{3+}$ species could be detected.

Single-crystal X-ray diffraction

X-ray quality single crystals were obtained for Nd^{III} and Yb^{III} analogues of $Zn_{16}Ln(quinoHA)_{16}$. The molecular structure of $Zn_{16}Yb(quinoHA)_{16}$ as obtained from X-ray single crystal diffraction is shown in Fig. 1, while that of $Zn_{16}Nd(quinoHA)_{16}$ is in Fig. S5.† Both compounds crystallize in the tetragonal space group $P4/ncc$. The structures of both MCs reveal the encapsulation of a Ln^{III} ion within the Zn_{16} shell, with the complexes having the general formula of $Ln^{III}[12\text{-}MC_{Zn(II), quinoHA}\text{-}4]_2[24\text{-}MC_{Zn(II), quinoHA}\text{-}8]$. The 6-coordinate Zn^{II} ions of the $[24\text{-}MC_{Zn(II), quinoHA}\text{-}8]$ ring are crystallographically equivalent, and each of them is coordinated by three O atoms and two N atoms from the hydroxime ligands and one N atom from the pyridine. The Zn^{II} ions of the two $[12\text{-}MC_{Zn(II), quinoHA}\text{-}4]$ rings are pyridine-free, 5-coordinated and adopt a distorted square pyramidal geometry. The Ln^{III} ion is sandwiched between two $[12\text{-}MC_{Zn(II), quinoHA}\text{-}4]$ rings and further encapsulated by a $[24\text{-}MC_{Zn(II), quinoHA}\text{-}8]$. The MC molecule has a crystallographic S_8 symmetry. Each Ln^{III} ion is coordinated by eight O atoms from two $[12\text{-}MC_{Zn(II), quinoHA}\text{-}4]$ rings. No solvent molecule is coordinated directly to Yb^{III} ion that adopts a square-antiprismatic coordination geometry around it, whilst 1.5 water molecules bound to Nd^{III} are observed and its coordination geometry is best described as a (bi)capped square antiprism.

NMR spectroscopy

Because of the paramagnetic nature of most Ln^{III} ions that induces fast relaxation and often causes strong line broadening in the NMR spectra, diamagnetic Y^{III} analogues ($Zn_{16}Y(HA)_{16}$) were prepared with both $napHA^{2-}$ and $quinoHA^{2-}$ families of ligands. Deuterated pyridine was used to prevent the observation of ^1H signals from the coordinated pyridine solvent molecules. ^1H and COSY-NMR spectra of $Zn_{16}Y(quinoHA)_{16}$ collected in DMSO-d_6 are shown in Fig. 2; the ones of $Zn_{16}Y(napHA)_{16}$ are provided in the ESI (Fig. S4†).

As can be seen from the crystal structure of Zn_{16}-$Yb(quinoHA)_{16}$, crystallographically inequivalent $quinoHA^{2-}$ ligands are present in the molecular architecture. The first group includes eight ligands of the two $[12\text{-}MC\text{-}4]$ and the second group contains the other eight ligands of the $[24\text{-}MC\text{-}8]$. The ^1H NMR spectrum of $Zn_{16}Y(quinoHA)_{16}$ displays, therefore, the presence of both types of $quinoHA^{2-}$ ligands in the ratio of 1 : 1. The NMR peaks were assigned as represented in Fig. 2 (top), in agreement with the presence of a total of 10 protons belonging to the two $quinoHA^{2-}$. This peak assignment was confirmed by the acquisition of an ^1H–^1H COSY-NMR spectrum Fig. 2 (bottom), which allows the determination of neighboring protons exhibiting correlations due to spin–spin coupling. Identical NMR spectra were obtained for the same samples after one week, confirming the long-term stability in solution of the $Zn_{16}Ln(HA)_{16}$ complexes.

Photophysical properties

Ligand-centered photophysical properties. $H_2quinoHA$ and H_2napHA hydroxamic acids exhibit absorption bands in the UV region which extend to the visible range up to 450 nm for the

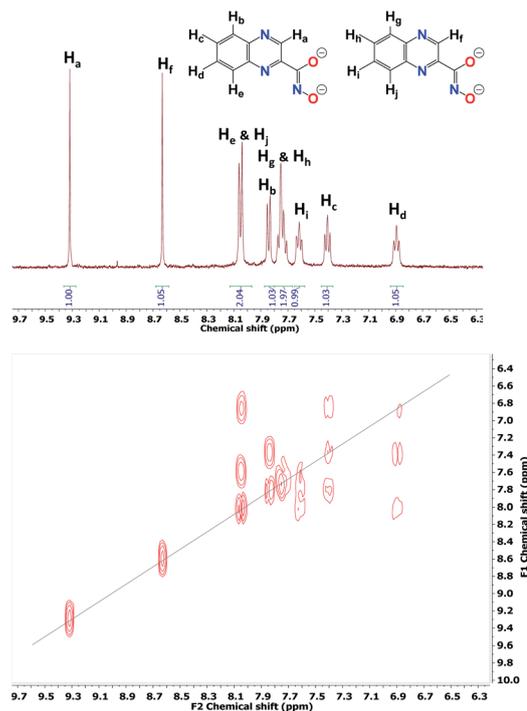Fig. 2 (top) ^1H-NMR spectrum and (bottom) ^1H–^1H COSY-NMR spectrum of $Zn_{16}Y$-quinoHA acquired in DMSO-d_6.

latter. These bands can be mainly attributed to $\pi \rightarrow \pi^*$ transitions (Fig. 3, black traces) on the basis of their extinction coefficients. It is important to note that, taking into account the heteroaromatic nature of the chromophoric moieties, the contribution of $n \rightarrow \pi^*$ transitions to the absorption bands should not be excluded.[42] From the edge of the absorption spectra, the positions of the lowest singlet state (S_1) were found to be located at 380 nm (26 320 cm^{-1}) and 447 nm (22 370 cm^{-1}) for $H_2quinoHA$ and H_2napHA, respectively (Table S4†). The deprotonation and the formation of $Zn_{16}Ln(HA)_{16}$ complexes induce a blue shift of the $\pi \rightarrow \pi^*$ absorption bands and the apparition of a new intra-ligand charge transfer (ILCT) band in the (near-)visible range which extends up to 490 nm and 510 nm
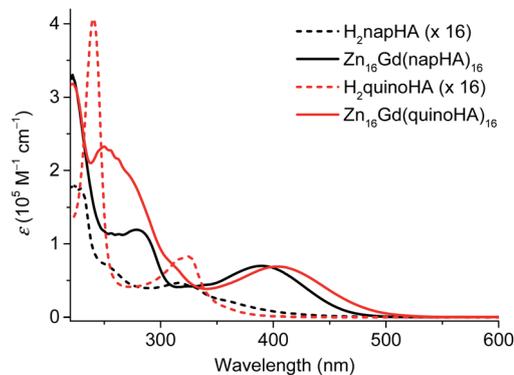

Fig. 3 Absorption spectra of hydroxamic acids (multiplied by a factor of 16) and of $Zn_{16}Gd(HA)_{16}$ (HA = $quinoHA^{2-}$, $napHA^{2-}$) recorded in CH_3OH at room temperature.
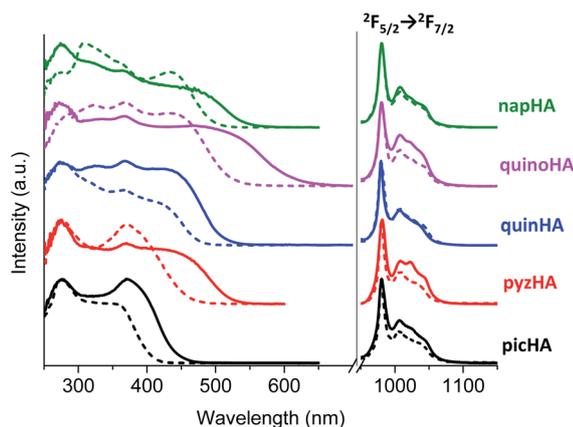
Fig. 4 (left) Excitation (λ_{em} = 980 nm) and (right) emission (λ_{ex} = 320–420 nm) spectra of $Zn_{16}Yb(HA)_{16}$ measured in the solid state (solid traces), or in 200 μM solutions in CH_3OH (HA = $picHA^{2-}$, $napHA^{2-}$, $quinoHA^{2-}$) or H_2O (HA = $pyzHA^{2-}$) (dashed traces) at room temperature.
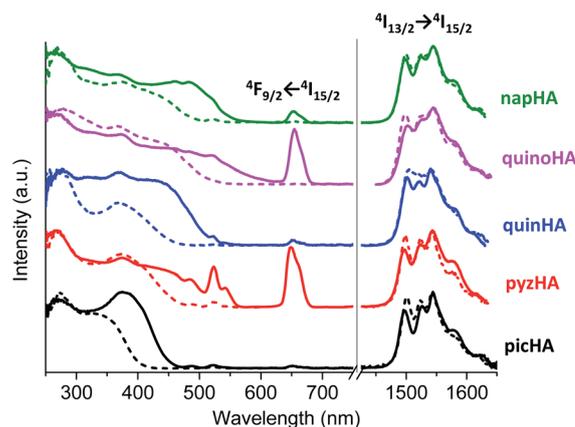

Fig. 6 (left) Excitation (λ_{em} = 1525 nm) and (right) emission (λ_{ex} = 320–420 nm) spectra of $Zn_{16}Er(HA)_{16}$ collected on solid state samples (solid traces), or in 1 mg mL^{-1} solutions in methanol (HA = $picHA^{2-}$, $quinoHA^{2-}$, $napHA^{2-}$, $quinoHA^{2-}$) or in water (HA = $pyzHA^{2-}$) (dashed traces) at room temperature.

for $Zn_{16}Ln(napHA)_{16}$ and $Zn_{16}Ln(quinoHA)_{16}$, respectively (Fig. 3, red traces). The positions of the apparent maxima appear at 387 nm (ε_{387} = 68 290 M^{-1} cm^{-1}) for $Zn_{16}Ln(napHA)_{16}$ and at 402 nm (ε_{402} = 73 370 M^{-1} cm^{-1}) for $Zn_{16}Ln(quinoHA)_{16}$. The molar absorption coefficients of $Zn_{16}Ln(HA)_{16}$ assembled using $picHA^{2-}$, $pyzHA^{2-}$, and $quinHA^{2-}$ ligands are summarized in Table S3,† while a comparison of absorption spectra is presented in Fig. 8.

Energy diagram. Since the sensitization of the characteristic emission of Ln^{III} ions in coordination compounds usually occurs through the 'antenna effect', the positions of ligand-centered electronic levels, in particular the lowest singlet (S_1), triplet (T_1) and ILCT states in respect to the accepting levels of Ln^{III}, are of particular importance.[43–46] The specific energies of the ILCT states were determined from the lower energy edge of the absorption spectra of $Zn_{16}Ln(HA)_{16}$ and were found to be located at 19 685 cm^{-1} (508 nm) for $Zn_{16}Ln(quinoHA)_{16}$ and

20 830 cm^{-1} (480 nm) for $Zn_{16}Ln(napHA)_{16}$. Corresponding Gd^{III} complexes are often used to determine the position of the T_1 state since the energy of the $^6P_{7/2}$ level (32 100 cm^{-1})[47] is too high to be populated through the energy levels of most organic ligands. Moreover, the heavy-atom and paramagnetic effects of Gd^{III} facilitate intersystem-crossing. The corresponding Zn_{16}-$Gd(HA)_{16}$ complexes were synthesized and their emission spectra in the solid state were analyzed. It was observed that the excitation into ILCT bands does not produce any detectable emission at room temperature or at 77 K. Higher energy excitation wavelengths at 290–320 nm, upon application of a time delay after the excitation flash, allowed us to collect phosphorescence spectra (Fig. S7†) and to determine the positions of the T_1 states: 24 150 cm^{-1} (414 nm) for $Zn_{16}Ln(quinoHA)_{16}$ and 25 510 cm^{-1} (392 nm) for $Zn_{16}Ln(napHA)_{16}$. (Table S4†). The diagram with the relative positions of the singlet, triplet and ILCT states for $Zn_{16}Ln(HA)_{16}$ as well as of the accepting energy levels of Yb^{III}, Nd^{III} and Er^{III} is shown in Fig. 9.
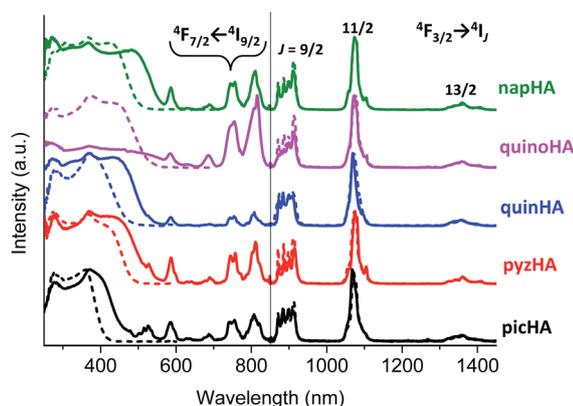

Fig. 5 (left) Excitation (λ_{em} = 1064 nm) and (right) emission (λ_{ex} = 320–420 nm) spectra of $Zn_{16}Nd(HA)_{16}$ collected on solid state samples (solid traces), in 1 mg mL^{-1} solutions in methanol (HA = $picHA^{2-}$, $quinoHA^{2-}$, $napHA^{2-}$, $quinoHA^{2-}$) or in water (HA = $pyzHA^{2-}$) (dashed traces) at room temperature.
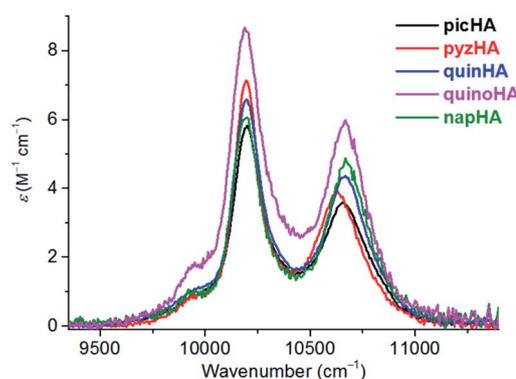

Fig. 7 Absorption spectra of $Zn_{16}Yb(HA)_{16}$ MCs measured in the energy range of the $^2F_{5/2} \leftarrow {}^2F_{7/2}$ transition in CH_3OH (HA = $picHA^{2-}$, $quinHA^{2-}$, $napHA^{2-}$, $quinoHA^{2-}$) or in H_2O (HA = $pyzHA^{2-}$) at room temperature (1.25–5.1 mM).
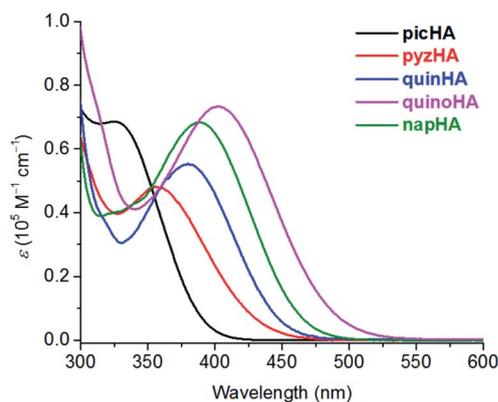
Fig. 8 Comparison of absorption spectra of $Zn_{16}Yb(HA)_{16}$ (HA = $picHA^{2-}$, $quinHA^{2-}$, $napHA^{2-}$, $quinoHA^{2-}$) or H_2O (HA = $pyzHA^{2-}$) collected in CH_3OH solutions at room temperature.

Ln^{III}-centered photophysical properties. Luminescence spectra were recorded for $Zn_{16}Ln(HA)_{16}$ (Ln = Yb^{III}, Nd^{III}, Er^{III}; HA = $quinoHA^{2-}$, $napHA^{2-}$) in the solid state and in CH_3OH and CD_3OD solutions under excitation in the range of 320–420 nm. All studied MCs exhibit intense Ln^{III}-centered emission in the NIR range arising from the $^2F_{5/2} \rightarrow {}^2F_{7/2}$, $^4F_{3/2} \rightarrow {}^4I_J$ (J = 9/2, 11/2, 13/2), and $^4I_{13/2} \rightarrow {}^4I_{15/2}$ transitions for Yb^{III} (Fig. 4, right), Nd^{III} (Fig. 5, right) and Er^{III} (Fig. 6, right) analogues, respectively. Excitation spectra of $Zn_{16}Yb(HA)_{16}$ MCs measured in the solid state and in solution upon monitoring the emission at 980 nm are dominated by ligand-centered broad bands. As Yb^{III} does not possess any electronic levels located in the UV-visible range, this result indicates the presence of an efficient sensitization of Yb^{III} emission through the electronic structure of the MC scaffold (Fig. 4, left). In the excitation spectra of $Zn_{16}Nd(HA)_{16}$ (Fig. 5, left) and $Zn_{16}Er(HA)_{16}$ (Fig. 6, left) MCs collected in the solid state, characteristic sharp intra-configurational f–f transitions could also be observed in addition to broad ligand-centered bands. The intensities of f–f transitions are similar to those of ligand-centered bands for
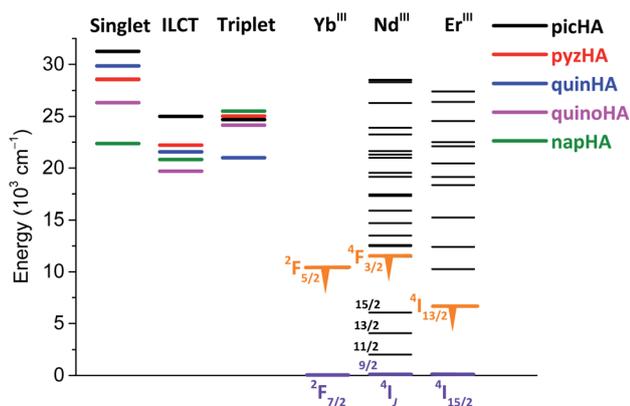
Nd^{III} and Er^{III} MCs formed with the $quinoHA^{2-}$ ligand but are weaker for the corresponding $Zn_{16}Ln(napHA)_{16}$ MCs. Such observations point to the possibility of sensitizing the characteristic Nd^{III} and Er^{III} emission not only through the MC scaffold but also through the direct excitation of f–f transitions. In solution, f–f transitions are undetectable and the excitation spectra of $Zn_{16}Nd(HA)_{16}$ (Fig. 5, left) and $Zn_{16}Er(HA)_{16}$ (Fig. 6, left) MCs are dominated by broad ligand-centered bands. For all analyzed MCs, profiles of the excitation spectra collected in solutions are matching those of the corresponding absorption spectra (Fig. 7 and S6†) while in the solid state, a broadening combined with an extension of the bands to the red domain up to 550 nm for $Zn_{16}Ln(napHA)_{16}$ and 630 nm for Zn_{16}-Ln(quinoHA)$_{16}$ is observed. Expanded excitation ranges for solid state samples compared to those obtained in solution can be explained by saturation effects.[48,49]

Ln^{III}-centered quantum yields (Q_{Ln}^L) and observed luminescence lifetimes (τ_{obs}) (Table 1) were collected under ligand excitation for all $Zn_{16}Ln(HA)_{16}$ in the solid state and in CH_3OH and CD_3OD solutions at room temperature. Using phenomenological equations[50,51] and values of τ_{obs} obtained in CH_3OH and CD_3OD solutions, we can confirm that no solvent molecules are directly coordinated to Yb^{III} or Nd^{III} in $Zn_{16}Ln(quinoHA)_{16}$ and in $Zn_{16}Ln(napHA)_{16}$. This result suggests that in the case of $Zn_{16}Nd(quinoHA)_{16}$ in CH_3OH and CD_3OD solutions, water molecules coordinated to Nd^{III} are dissociated while the coordination of larger solvent molecules is sterically hindered.

In addition, for all Nd^{III} and Er^{III} samples of the Zn_{16}-Ln(HA)$_{16}$ family, their intrinsic quantum yields (Q_{Ln}^{Ln}) were measured in the solid state under direct excitation into the $^4F_{7/2} \leftarrow {}^4I_{9/2}$ transition at 750 nm for $Zn_{16}Nd(HA)_{16}$ and the $^4F_{9/2} \leftarrow {}^4I_{15/2}$ transition located at 650 nm for $Zn_{16}Er(HA)_{16}$. Taking into account Q_{Ln}^L, Q_{Ln}^{Ln} and τ_{obs} for Nd^{III} and Er^{III} samples in the solid state, the values of τ_{rad} and η_{sens} were calculated according to eqn (1). It has been shown previously that these MCs remain intact in solution. Therefore, τ_{rad} were adjusted for the differences in refractive indexes (n), i.e. τ_{rad}(solution) = τ_{rad}(solid state) $\times (n_{solid\ state}/n_{solution})^3$.[29] In the solid state, the refractive index was set to be equal to 1.5, while the $n_{solution}$ values are admitted to be the ones of the neat solvents, e.g. $n(CD_3OD)$ = 1.326; $n(CH_3OH)$ = 1.329; $n(D_2O)$ = 1.328; $n(H_2O)$ = 1.34.

For $Zn_{16}Yb(HA)_{16}$ MCs, intrinsic quantum yields could not be measured experimentally. However, Yb^{III} electronic transitions generating the luminescence terminate in the ground level. Therefore, if the absorption spectrum corresponding to the emission spectrum is known, τ_{rad} can be calculated using the modified Einstein's equation (eqn (2a) and (2b)):[52]

$$\frac{1}{\tau_{rad}} = 2303 \times \frac{8\pi c n^2 \tilde{\nu}_m^2 (2J + 1)}{N_A (2J' + 1)} \int \varepsilon(\tilde{\nu}) d\tilde{\nu} \qquad (2a)$$

$$\tilde{\nu}_m = \frac{\int \tilde{\nu} \varepsilon(\tilde{\nu}) d\tilde{\nu}}{\int \varepsilon(\tilde{\nu}) d\tilde{\nu}} \qquad (2b)$$

where c is the speed of light in centimeters per second, n is the refractive index, N_A is Avogadro's number, J and J' are the

Fig. 9 Schematic energy diagram showing the energy positions of singlet states in H_2HA, as well as triplet and ILCT levels in $Zn_{16}Gd(HA)_{16}$ in respect to the accepting energy levels of NIR-emitting Yb^{III}, Nd^{III}, Er^{III} ions.

Table 1 Photophysical parameters for $Zn_{16}Ln(HA)_{16}$ in the solid state and in 200 μM solutions in methanol (HA = $picHA^{2-}$, $quinHA^{2-}$, $napHA^{2-}$, $quinoHA^{2-}$) or water (HA = $pyzHA^{2-}$)[a]

Compound	State/solvent	τ_{obs}[b] (μs)	τ_{rad}[c] (μs)	Q_{Ln}^{Ln}[c] (%)	Q_{Ln}^{L}[d] (%)	η_{sens}[c] (%)
$Zn_{16}Yb(picHA)_{16}$	Solid	34.5(1)	410	8.4	0.40(2)	4.8
	CH_3OH	12.1(1)	524	2.3	0.13(1)	5.6
	CD_3OD	133(1)	526	25.3	1.60(3)	6.3
$Zn_{16}Nd(picHA)_{16}$	Solid	1.18(2)	293	0.40(9)	0.40(1)	~100
	CH_3OH	0.90(1)	375	0.24	0.22(2)	92
	CD_3OD	3.53(1)	377	0.94	0.98(1)	~100
$Zn_{16}Er(picHA)_{16}$	Solid	3.47(4)	11.8×10^3	$2.95(9) \times 10^{-2}$	$1.34(4) \times 10^{-2}$	45
	CH_3OH	1.02(1)	15.1×10^3	6.75×10^{-3}	$1.30(3) \times 10^{-3}$	19
	CD_3OD	10.4(1)	15.2×10^3	6.8×10^{-2}	$5.24(6) \times 10^{-2}$	77
$Zn_{16}Yb(pyzHA)_{16}$	Solid	45.6(3)	399	11.4	0.659(4)	5.8
	H_2O	5.57(1)	499	1.12	$1.12(7) \times 10^{-2}$	1.0
	D_2O	81.3(1)	508	16	0.257(3)	1.6
$Zn_{16}Nd(pyzHA)_{16}$	Solid	1.71(1)	133	1.82(3)	0.444(9)	34
	H_2O	0.214(4)	166	0.13	$7.7(1) \times 10^{-3}$	6.0
	D_2O	1.29(1)	169	0.76	$6.17(9) \times 10^{-2}$	8.1
$Zn_{16}Er(pyzHA)_{16}$	Solid	4.96(4)	3.82×10^3	0.130(6)	$9.5(2) \times 10^{-3}$	7.3
	D_2O	7.02(2)	4.91×10^3	0.14	$1.70(4) \times 10^{-3}$	1.2
$Zn_{16}Yb(quinHA)_{16}$	Solid	47.8(4)	530	9.0	2.44(4)	27
	CH_3OH	14.88(1)	675	2.2	0.25(1)	11.3
	CD_3OD	150.7(2)	679	22	2.88(2)	13.0
$Zn_{16}Nd(quinHA)_{16}$	Solid	1.79(2)	166	1.54(4)	1.13(4)	~100
	CH_3OH	1.16(1)	212	0.55	0.38(1)	69
	CD_3OD	4.11(2)	214	1.9	1.35(1)	70
$Zn_{16}Er(quinHA)_{16}$	Solid	5.73(2)	3.58×10^3	0.16(1)	$4.2(1) \times 10^{-2}$	26.3
	CH_3OH	1.25(1)	4.58×10^3	2.7×10^{-2}	$9.9(3) \times 10^{-4}$	3.6
	CD_3OD	11.40(3)	4.6×10^3	0.25	$3.6(1) \times 10^{-2}$	14.5
$Zn_{16}Yb(quinoHA)_{16}$	Solid	49.7(2)	250	19.9	0.637(5)	3.2
	CH_3OH	22.6(1)	320	7.1	0.135(1)	1.9
	CD_3OD	124.0(1)	322	38	0.88(2)	2.3
$Zn_{16}Nd(quinoHA)_{16}$	Solid	1.04(1)[e]	202	0.51(1)	0.153(2)	30
	CH_3OH	0.79(1)	259	0.31	$7.1(1) \times 10^{-2}$	23
	CD_3OD	1.50(1)	261	0.57	0.160(5)	28
$Zn_{16}Er(quinoHA)_{16}$	Solid	5.89(2)	7.46×10^3	$7.9(1) \times 10^{-2}$	$1.11(5) \times 10^{-2}$	14.1
	CH_3OH	1.32(1)	9.55×10^3	1.3×10^{-2}	$3.7(3) \times 10^{-4}$	2.7
	CD_3OD	10.8(1)	9.61×10^3	0.11	$9.8(2) \times 10^{-3}$	8.7
$Zn_{16}Yb(napHA)_{16}$	Solid	41.3(2)	351	11.8	1.10(2)	9.3
	CH_3OH	20.0(1)	454	4.4	0.156(3)	3.5
	CD_3OD	159(1)	456	35	1.57(3)	4.5
$Zn_{16}Nd(napHA)_{16}$	Solid	1.13(1)	139	0.82(2)	0.34(1)	41
	CH_3OH	0.993(4)	178	0.56	0.168(3)	30
	CD_3OD	3.73(3)	180	2.1	0.731(3)	35
$Zn_{16}Er(napHA)_{16}$	Solid	3.96(1)	4.21×10^3	$9.4(3) \times 10^{-2}$	$1.29(1) \times 10^{-2}$	13.7
	CH_3OH	1.27(1)	5.39×10^3	2.3×10^{-2}	$5.2(4) \times 10^{-4}$	2.2
	CD_3OD	11.7(1)	5.41×10^3	0.22	$1.88(2) \times 10^{-2}$	8.7

[a] Data at room temperature. Standard deviation (2σ) between parentheses; estimated relative errors: τ_{obs}, ±2%; τ_{rad}, ±10–12%; Q_{Ln}^{L}, ±10%; Q_{Ln}^{Ln}, ±10–12%; η_{sens}, ±22%. [b] Under excitation at 355 nm. [c] See text for details. [d] Under excitation at 320–420 nm. [e] Average lifetime calculated from $\tau_1 = 1.12(1)$ μs (74%); $\tau_2 = 0.39(1)$ μs (26%).

quantum numbers for the ground and the excited states, respectively, $\int \varepsilon(\tilde{\nu})d\tilde{\nu}$ is the integrated spectrum of the $^2F_{5/2} \leftarrow$ $^2F_{7/2}$ transition, $\tilde{\nu}_m$ is the barycenter of the transition. The corresponding absorption spectra were measured for all Zn_{16}-$Yb(HA)_{16}$ (Fig. 7). The resulting τ_{obs} values were adjusted to the media based on the difference in refractive indexes, as explained before, and used to calculate Q_{Ln}^{Ln} and η_{sens} according to eqn (1).

All quantitative photophysical parameters are summarized in Table 1 and presented on Fig. 10.

Discussion

MCs with the general formula, $Ln^{III}[12-MC_{Zn(II),HA}-4]_2[24-MC_{Zn(II),HA}-8]$ ($Zn_{16}Ln(HA)_{16}$, Ln^{III} = Yb, Nd, Er, Gd & Y; HA = $picHA^{2-}$, $pyzHA^{2-}$, $quinHA^{2-}$, $quinoHA^{2-}$, $napHA^{2-}$) can be obtained by self-assembly reactions between the corresponding hydroxamic acid, Zn^{II} and Ln^{III} triflates in an appropriate molar ratio. Although the general synthetic strategy is the same, the solvents and the base used in the reactions have to be adjusted according to the nature of the hydroxamic acid. In the case of MCs formed with $picHA^{2-}$ and $quinHA^{2-}$, an addition of
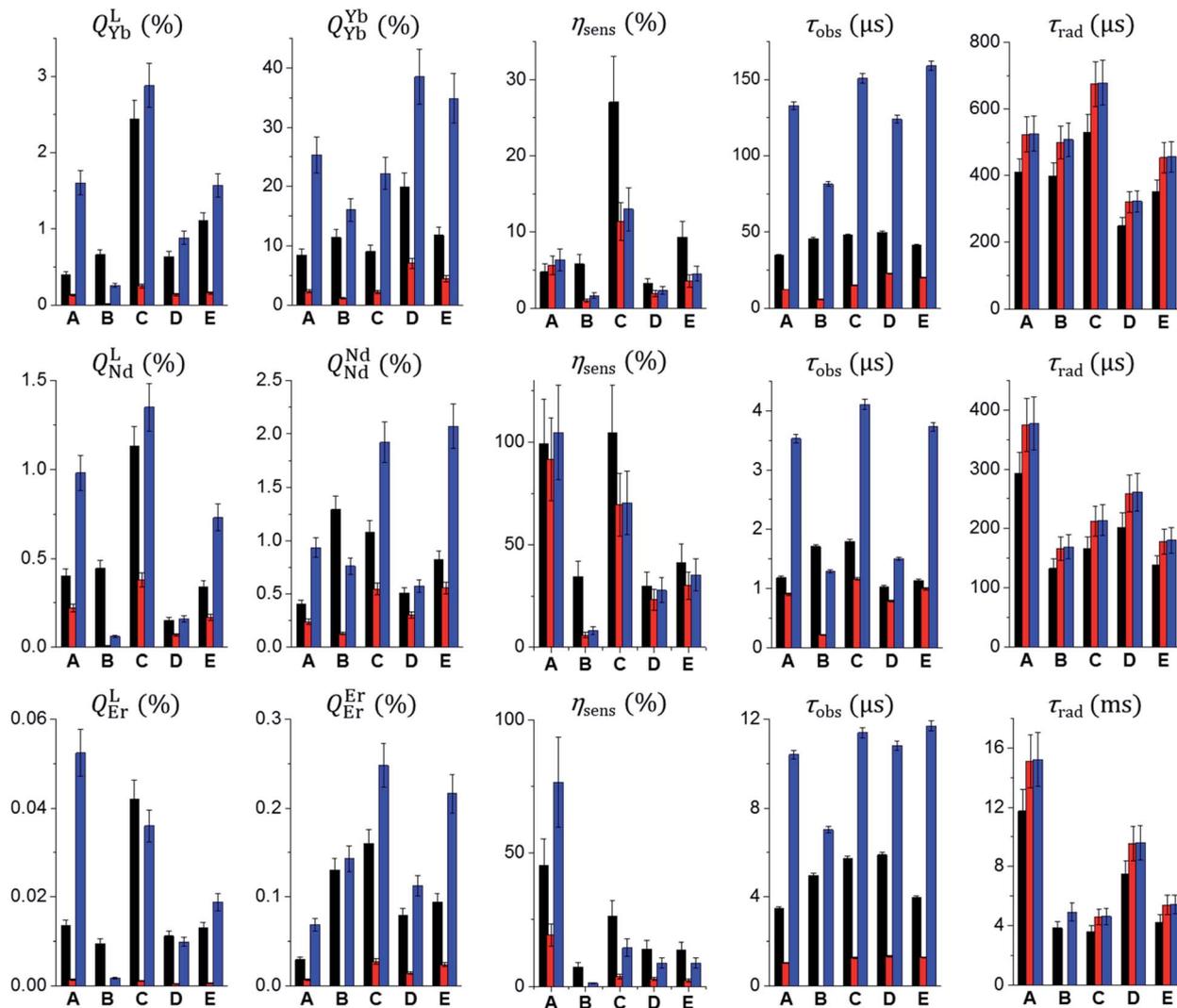
Fig. 10 Comparison of total and intrinsic quantum yields, sensitization efficiencies, observed and radiative lifetimes for $Zn_{16}Ln(HA)_{16}$ (Ln = Yb[III], Nd[III], Er[III]; HA = picHA[2−] (A), pyzHA[2−] (B), quinHA[2−] (C), quinoHA[2−] (D), napHA[2−] (E)) in the solid state (black bars) or solution in CH_3OH or H_2O (red bars) and CD_3OD or D_2O (blue bars).

sodium hydroxide or trimethylamine is necessary to ensure the formation of the desired $Zn_{16}Ln(HA)_{16}$ (ref. 32 and 33) while MCs formed with pyzHA[2−],[37] quinoHA[2−] and napHA[2−] can be obtained in the presence of pyridine in H_2O or in a H_2O/DMF mixture, respectively. The crystal structures of all studied $Zn_{16}Ln(HA)_{16}$ MCs show that Ln[III] ion is sandwiched between two [12-MC$_{Zn(II),HA}$-4] and are further encapsulated by a [24-MC$_{Zn(II),HA}$-8] unit. The Ln[III] ion is bonded to four hydroximate oxygens of each of the [12-MC$_{Zn(II),HA}$-4] motifs, forming a square antiprismatic coordination geometry. No solvent molecule is coordinated directly to the Ln[III] ion except for $Zn_{16}Nd(quinoHA)_{16}$ where 1.5 water molecules connected to Nd[III] were observed. Nevertheless, in general, the differences in the electronic structure of the hydroximate ligands have a minimal effect on the first coordination sphere around the Ln[III] ion, thus providing an opportunity to study systematically the effect of the nature of the ligand on the resulting photophysical properties of $Zn_{16}Ln(HA)_{16}$ MCs. In particular, we will

discuss how the nature of the hydroximate ligands forming the $Zn_{16}Ln(HA)_{16}$ scaffold affects absorption, excitation and emission spectra as well as the different quantitative photophysical parameters for the newly reported NIR-emitting Zn_{16}-$Ln(quinoHA)_{16}$ $Zn_{16}Ln(napHA)_{16}$ and the previously described $Zn_{16}Ln(picHA)_{16}$,[33] $Zn_{16}Ln(pyzHA)_{16}$ (ref. 37) and $Zn_{16}Ln(quinHA)_{16}$.[32]

First, we demonstrated that, by varying the nature of hydroxamic acids, *i.e.* the number of nitrogen atoms in the aromatic rings and the degree of conjugation, it is possible to tune the maxima of the low-energy ILCT bands in the absorption spectra of $Zn_{16}Ln(HA)_{16}$ from 330 nm (HA = picHA[2−]), 360 nm (HA = picHA[2−]), 380 nm (HA = pyzHA[2−]) to 387 nm (HA = napHA[2−]) and 402 nm (HA = quinoHA[2−]) (Fig. 8).

In view of the sensitization of Ln[III] emission, the mutual energy positions of the ligand-centered donating states and the accepting levels of Ln[III] are of particular importance.[20,43–46] In general, the sensitization process involves an energy transfer

originating from the triplet state of the chromophore unit. However, the population of Ln^{III} excited energy levels through singlet and charge transfer states located at lower energy should also be considered. The corresponding energy diagram for $Zn_{16}Ln(HA)_{16}$ and Yb^{III}, Nd^{III} and Er^{III} is presented in Fig. 9. Several features are important to note. In the case of MCs formed with $picHA^{2-}$ and $quinHA^{2-}$, the positions of the T_1 and the ILCT states are located very closely to each other with an energy difference which is less than 600 cm^{-1}, while the singlet state is located at least 6500 cm^{-1} higher in energy. For Zn_{16}-$Ln(pyzHA)_{16}$, $Zn_{16}Ln(quinoHA)_{16}$ and $Zn_{16}Ln(napHA)_{16}$, the T_1 state is positioned at a higher energy than the ILCT and the energy difference between these states is larger than 2800 cm^{-1}. Singlet states in $Zn_{16}Ln(pyzHA)_{16}$, $Zn_{16}Ln(quinoHA)_{16}$ are located higher in energy than the T_1 by values of 3535 cm^{-1} and 2170 cm^{-1}, respectively, while in $Zn_{16}Ln(napHA)_{16}$, the energy of S_1 state is lower than the one of T_1. The last observation can be explained by the different nature of these electronic states, *i.e.* $n\pi^*$ *vs.* $\pi\pi^*$. It should also be mentioned that the positions of the singlet states were determined from the edge of the absorption spectra of the corresponding hydroxamic acids and that their energies may shift in $Zn_{16}Ln(HA)_{16}$. Nevertheless, one can see that for all studied $Zn_{16}Ln(HA)_{16}$ MCs, the ligand-centered levels are located higher in energy than the $^2F_{5/2}$, $^4F_{3/2}$ and $^4I_{13/2}$ levels of Yb^{III}, Nd^{III} and Er^{III}, respectively, so all can act as potential sensitizers of their characteristic NIR emission.

Excitation spectra of all the studied $Zn_{16}Yb(HA)_{16}$ MCs collected in the solid state and in solution upon monitoring the Yb^{III} emission at 980 nm are dominated by broad ligand-centered bands indicating an efficient sensitization of Yb^{III} emission through the electronic structure of the MC scaffold (Fig. 4, left). The excitation spectra of $Zn_{16}Nd(HA)_{16}$ (Fig. 5, left) and $Zn_{16}Er(HA)_{16}$ (Fig. 6, left) MCs in the solid state reveal the presence of sharp bands that correspond to f–f transitions in addition to the broad ligand-centered bands. Their intensities depend on the nature of the hydroxamic acid. The excitation spectrum of $Zn_{16}Nd(quinoHA)_{16}$ is dominated by the sharp bands arising from the f–f transitions while their intensities are significantly less important for $Zn_{16}Nd(quinHA)_{16}$. Among Er^{III} MCs, f–f transitions have the lowest intensities for Zn_{16}-$Er(picHA)_{16}$ and $Zn_{16}Er(quinHA)_{16}$ while they have the highest intensities for $Zn_{16}Er(pyzHA)_{16}$ and $Zn_{16}Er(quinoHA)_{16}$. Such observations indicate that the sensitization of the characteristic Nd^{III} and Er^{III} emissions for $Zn_{16}Ln(HA)_{16}$ in the solid state may not only occur through the MC scaffold but also through direct excitation of f–f transitions. In solution, the excitation spectra of all $Zn_{16}Nd(HA)_{16}$ and $Zn_{16}Er(HA)_{16}$ MCs exhibit only the presence of ligand-centered bands and no f–f transitions could be detected.

Upon excitation into the ILCT bands in the range of 320–420 nm, all the studied $Zn_{16}Ln(HA)_{16}$ MCs exhibit characteristic Ln^{III} emission in the NIR range. For Yb^{III} MCs, emission bands are observed in the range of 950–1060 nm and originate from the $^2F_{5/2} \rightarrow {}^2F_{7/2}$ transition (Fig. 4, right), while for Er^{III} bands appear in the range of 1450–1650 nm arising from the $^4I_{13/2} \rightarrow {}^4I_{15/2}$ transition (Fig. 6, right). The emission spectra of Zn_{16}-$Nd(HA)_{16}$ are dominated by the $^4F_{3/2} \rightarrow {}^4I_{11/2}$ transition in the

range of 1050–1120 nm, while two additional bands with lower intensities appear at 850–930 nm and 1300–1420 nm. They are assigned to $^4F_{3/2} \rightarrow {}^4I_{9/2}$ and $^4F_{3/2} \rightarrow {}^4I_{13/2}$ transitions, respectively (Fig. 5, right). It should be noted that for a specific Ln^{III} ion, the obtained emission spectra are almost independent of the nature of the hydroxamic acid forming the MC, reflecting the similarity of coordination environments around Ln^{III} which is in full agreement with the structural data (*vide supra*). Moreover, the emission spectra recorded for the $Zn_{16}Ln(HA)_{16}$ samples in the solid state and solutions are very similar by their bandwidths and crystal-field splitting as an additional indication that MCs remain intact in solution.

Experimental luminescence decay curves collected for most of the studied MCs in the solid state and solutions are best fitted with mono-exponential functions, reflecting the presence of only one emissive Ln^{III}-containing species. The sole exception has been observed with $Zn_{16}Nd(quinoHA)_{16}$ in the solid state for which a bi-exponential luminescence decay was observed with corresponding 'long' (1.12(1) μs) and 'short' (0.39(1) μs) τ_{obs} values. The 'short' component corresponds most probably to MCs containing 1.5 water molecules directly coordinated to Nd^{III} (as observed in the crystal structure of this MC, *vide supra*), while the 'long' component correspond to the Zn_{16}-$Nd(quinoHA)_{16}$ that doesn't contain H_2O molecules directly coordinated to Nd^{III}. Luminescence decays collected on CH_3OH and CD_3OD solutions of $Zn_{16}Nd(quinoHA)_{16}$ are mono-exponential, indicating that coordinated to Nd^{III} water molecules are dissociated while the coordination of other solvent molecules is sterically hindered. Observed luminescence life-times (τ_{obs}, Table 1) significantly decrease when going from the solid state samples to solutions in CH_3OH or H_2O (Fig. 10, black and red bars) reflecting a detrimental effect of O–H and C–H vibrations on non-radiative deactivation of the NIR-emitting Ln^{III} ions.[12] The latter is also revealed in a pronounced (2–15 times) lengthening of τ_{obs} values for solutions of MCs in deuterated solvents (Fig. 10, blue bars). The use of phenomenological equations[50,51] with the values of τ_{obs} recorded in CH_3OH and CD_3OD, or in H_2O and D_2O solutions for Zn_{16}-$Yb(HA)_{16}$ and $Zn_{16}Nd(HA)_{16}$ confirmed that no solvent molecules are directly coordinated to either Yb^{III} or Nd^{III} within the whole series of studied MCs, indicating that shortening of τ_{obs} values is induced by non-radiative deactivations through second-sphere interactions with overtones of O–H and C–H vibrations.

Values of τ_{obs} recorded on solutions of $Zn_{16}Yb(HA)_{16}$ and $Zn_{16}Nd(HA)_{16}$ in deuterated solvents are longer compared to these collected in CH_3OH and H_2O which results in a comparable enhancement of the Q_{Ln}^{Ln} and Q_{Ln}^{L} values. On the other hand, for $Zn_{16}Er(HA)_{16}$ in CD_3OD solution the τ_{obs} and Q_{Er}^{Er} values are 8–10 times larger compared to the values obtained in CH_3OH, while the Q_{Er}^{L} values increase by 26–40 times. An explanation can be found in the values of sensitization efficiencies (η_{sens}) that are similar for solutions of Yb^{III} and Nd^{III} MCs in protic and deuterated solvents while at least a 3-times enhancement is observed for the values of Er^{III} collected in CD_3OD. In general, the lowest values of Q_{Ln}^{L} are obtained for solutions of $Zn_{16}Ln(HA)_{16}$ in CH_3OH and in H_2O. The

comparison of Q_{Ln}^L values for $Zn_{16}Ln(HA)_{16}$ samples in the solid state and in solution in deuterated solvents (Fig. 10, black and blue bars) revealed different trends depending on the nature of the hydroxamic acid. Similar values of Q_{Ln}^L are observed for $Zn_{16}Ln(quinHA)_{16}$ and $Zn_{16}Ln(quinoHA)_{16}$, since the higher values of τ_{obs} and Q_{Ln}^{Ln} in CD_3OD solutions are compensated by a comparable enhancement of the sensitization efficiency in the solid state. For $Zn_{16}Ln(pyzHA)_{16}$, the values of η_{sens} are 3.6–6.1 times larger in the solid state than in D_2O solutions leading to a significantly improved value of Q_{Ln}^L for the former. In the case of $Zn_{16}Ln(picHA)_{16}$ and $Zn_{16}Ln(napHA)_{16}$, Q_{Ln}^L are lower for samples in the solid state vs. solution in CD_3OD since the values of η_{sens} are similar or lower in the solid state. Thus, the non-radiative deactivation of Ln^{III} NIR emission through O–H and C–H vibrations in solutions of MCs in protic solvents has a dominating role and negatively impact the main quantitative characteristics. On the other hand, the values of Q_{Ln}^L for samples of $Zn_{16}Ln(HA)_{16}$ in the solid state and in deuterated solvents depend on the nature of the hydroxymate ligand and Ln^{III} ion.

Several points should be highlighted if we consider further the effect of the nature of the hydroxymate ligands on the quantitative photophysical parameters of $Zn_{16}Ln(HA)_{16}$ in the solid state. For a specific Ln^{III} ion, the values of τ_{obs} are within a relatively narrow range, i.e. 34.5–49.7 μs for Yb^{III}, 1.04–1.79 μs for Nd^{III} and 3.47–5.89 μs for Er^{III} MCs. Considering the similarity of the crystal structures, such variations are mainly caused by the coordination of water molecules (for $Zn_{16}Nd(quinoHA)_{16}$) or by the presence of sources of non-radiative deactivations through co-crystallized solvent molecules. On the other hand, the effect of the nature of the hydroxymate ligand on τ_{rad} values is more pronounced. Changes as significant as >3-fold are detected in the case of $Zn_{16}Er(picHA)_{16}$ (11.8 ms) vs. $Zn_{16}Er(quinHA)_{16}$ (3.58 ms) or $Zn_{16}Er(pyzHA)_{16}$ (3.82 ms). Among Nd^{III} MCs, the longest τ_{rad} value is observed for $Zn_{16}Nd(picHA)_{16}$ (293 μs) and the shortest for $Zn_{16}Nd(pyzHA)_{16}$ (133 μs). For Yb^{III} MCs, the variation of the τ_{rad} values is also significant, from 530 μs for $Zn_{16}Yb(quinHA)_{16}$ to 250 μs for $Zn_{16}Yb(quinoHA)_{16}$. So, despite the highly similar coordination environments (through eight oxygen atoms) and symmetry (square antiprism) around the Ln^{III} ions in $Zn_{16}Ln(HA)_{16}$, the nature of the hydroxymate ligand appears to impact radiative lifetimes. An enhanced understanding of the factors that control this parameter is important for the design of highly luminescent Ln^{III} compounds since the shorter τ_{rad} leads to a higher Q_{Ln}^{Ln} (Eq. (1)). The validity of this approach has been demonstrated in several studies.[26,29–31] Indeed, values of Q_{Ln}^{Ln} are the highest for Nd^{III} (1.5–1.8%) and Er^{III} (0.13–0.16%) MCs formed with $pyzHA^{2-}$ and $quinHA^{2-}$, while in the case of Yb^{III} for MCs formed with $quinoHA^{2-}$ (19.9%), all of them correspond to the lowest values of τ_{rad}. Another important parameter that is largely affected by the nature of the hydroxymate ligand is the sensitization efficiency. It varies from 4.8 to 27%, from 30 to 100%, and from 7.3 to 45% for $Zn_{16}Yb(HA)_{16}$, $Zn_{16}Nd(HA)_{16}$ and $Zn_{16}Er(HA)_{16}$, respectively. The highest values of η_{sens} have been found in Yb^{III} MCs formed with $quinHA^{2-}$ and in $Zn_{16}Er(picHA)_{16}$. The scaffolds of both MCs sensitize equally well the characteristic emission of Nd^{III} with a η_{sens} of ∼100%. Here,

a correlation with the mutual positions of the ILCT and the triplet states can be followed (vide supra). In particular, these energy states are located very close to each other in $Zn_{16}Ln(picHA)_{16}$ and in $Zn_{16}Ln(quinHA)_{16}$ while for other MCs, the energy of T_1 is higher than the one of the ILCT state. On the basis of the values of η_{sens}, a high proximity in energy positions of T_1 and ILCT should be preferred for the sensitization of the NIR-emitting Yb^{III}, Nd^{III} and Er^{III}. Finally, all these variations lead to the largest values of Q_{Ln}^L observed for $Zn_{16}Ln(quinHA)_{16}$ in the solid state.

Conclusions

In this work, we have extended the $Zn_{16}Ln(HA)_{16}$ 'encapsulated sandwich' family by creating MCs with two new ligands, naphthyridine- and quinoxaline-hydroximates. We have demonstrated how the nature of the hydroximate ligand impacts the photophysical properties of these MCs. In particular, by varying ligands from picoline-, pyrazine-, quinaldine-, naphthyridine- and quinoxaline-hydroximates, the low-energy ILCT bands present in the absorption spectra of $Zn_{16}Ln(HA)_{16}$ can be shifted from the UV to the visible range up to 510 nm and the corresponding maxima from 330 nm to 402 nm. MC scaffolds sensitize well the NIR characteristic emissions of Yb^{III}, Nd^{III} and Er^{III} ions in all studied $Zn_{16}Ln(HA)_{16}$ with total quantum yield values and observed luminescence lifetimes that are comparable to the highest values reported so far for Ln^{III} coordination compounds. The extensive detailed analysis of the quantitative photophysical parameters revealed that the values of Q_{Ln}^L, Q_{Ln}^{Ln}, η_{sens} and τ_{obs} depend on (i) the media, (ii) the nature of the Ln^{III} ion and (iii) the hydroximate ligands. The values of τ_{obs} are the longest collected for $Zn_{16}Ln(HA)_{16}$ in deuterated solvents followed by those measured in the solid state and in protic solvents. Considering that no solvent molecule is directly coordinated to Ln^{III} in solution, a negative effect of second-sphere non-radiative deactivation of Ln^{III} ions induced by overtones of O–H and C–H vibrations is significant. For a specific Ln^{III} ion, the measured values of Q_{Ln}^L are the highest for $Zn_{16}Yb(quinHA)_{16}$ and $Zn_{16}Nd(quinHA)_{16}$ in all media, for $Zn_{16}Er(quinHA)_{16}$ in the solid state and for $Zn_{16}Er(picHA)_{16}$ in solution. With few exceptions, the sensitization is more efficient in $Zn_{16}Ln(HA)_{16}$ samples in the solid state compared to the values measured in solutions and η_{sens} values as high as 100% are observed for $Zn_{16}Nd(picHA)_{16}$ and $Zn_{16}Nd(quinHA)_{16}$. Notably, for $Zn_{16}Ln(picHA)_{16}$ and $Zn_{16}Ln(quinHA)_{16}$, the energies of the triplet and the ILCT states are fairly similar ($\Delta E < 600$ cm^{-1}) while $E(T_1)$ is higher than $E(ILCT)$ for other MCs. Despite the similarities of the coordination environments and symmetries around Ln^{III} within the $Zn_{16}Ln(HA)_{16}$ family, radiative lifetimes of a specific Ln^{III} ion are not constant and are largely affected by the nature of hydroximate ligand. Finally, having all of these comprehensive data in hand, it is possible to rationally design and create $Zn_{16}Ln(HA)_{16}$ with desired photophysical properties suitable for NIR imaging applications. More detailed studies that combine time-resolved measurements with theoretical calculations are required to finalize the precise assignment of energy levels and to obtain a deeper level of

understanding of intricate energy transfer processes occurring in $Zn_{16}Ln(HA)_{16}$ which will be the subject of future reports.

Author contributions

Data availability

The experimental data that support the findings of this study are provided in ESI† and available online or upon reasonable request from the corresponding authors.

Conflicts of interest

There are no conflicts to declare.

Acknowledgements

Notes and references

1 S. He, J. Song, J. Qu and Z. Cheng, *Chem. Soc. Rev.*, 2018, **47**, 4258–4278.
2 Kenry, Y. Duan and B. Liu, *Adv. Mater.*, 2018, **30**, e1802394.
3 Q. Miao and K. Pu, *Adv. Mater.*, 2018, **30**, e1801778.
4 C. Wang, Z. Wang, T. Zhao, Y. Li, G. Huang, B. D. Sumer and J. Gao, *Biomat*, 2018, **157**, 62–75.
5 Y. Fan and F. Zhang, *Adv. Opt. Mater.*, 2019, **7**, 1801417.
6 I. Martinić, S. V. Eliseeva and S. Petoud, *J. Lumin.*, 2017, **189**, 19–43.
7 Y. Y. Ning, M. L. Zhu and J. L. Zhang, *Coord. Chem. Rev.*, 2019, **399**, 213028.
8 J.-C. G. Bünzli and S. V. Eliseeva, *J. Rare Earths*, 2010, **28**, 824–842.
9 L. Wang, Z. Zhao, C. Wei, H. Wei, Z. Liu, Z. Bian and C. Huang, *Adv. Opt. Mater.*, 2019, **7**, 1801256.
10 S. Comby and J.-C. G. Bünzli, in *Handbook on the Physics and Chemistry of Rare Earths*, ed. K. A. Gschneidner Jr, J.-C. G. Bünzli and V. K. Pecharsky, Elsevier Science B.V., Amsterdam, 2007, ch. 235, vol. 37, pp. 217–470.
11 J.-C. G. Bünzli and S. V. Eliseeva, in *Comprehensive Inorganic Chemistry II*, ed. V. W.-W. Yam, Elsevier B.V., Amsterdam, 2013, ch. 8.08, vol. 8, pp. 339–398.
12 J.-C. G. Bünzli and S. V. Eliseeva, in *Springer Series on Fluorescence. Lanthanide Luminescence: Photophysical, Analytical and Biological Aspects*, ed. P. Hänninen and H. Härmä, Springer Verlag, Berlin, 2011, vol. 7, pp. 1–45.
13 M. Latva, H. Takalo, V. M. Mukkala, C. Matachescu, J.-C. Rodriguez-Ubis and J. Kankare, *J. Lumin.*, 1997, **75**, 149–169.
14 R. D. Archer, H. Y. Chen and L. C. Thompson, *Inorg. Chem.*, 1998, **37**, 2089–2095.
15 S. Sato and M. Wada, *Bull. Chem. Soc. Jpn.*, 1970, **43**, 1955–1962.
16 M. H. V. Werts, R. H. Woudenberg, P. G. Emmerink, R. van Gassel, J. W. Hofstraat and J. W. Verhoeven, *Angew. Chem., Int. Ed.*, 2000, **39**, 4542–4544.
17 M. H. V. Werts, J. W. Hofstraat, F. A. J. Geurts and J. W. Verhoeven, *Chem. Phys. Lett.*, 1997, **276**, 196–201.
18 J.-Y. Hu, Y. Ning, Y.-S. Meng, J. Zhang, Z.-Y. Wu, S. Gao and J.-L. Zhang, *Chem. Sci.*, 2017, **8**, 2702–2709.
19 Y. Y. Ning, J. Tang, Y. W. Liu, J. Jing, Y. S. Sun and J. L. Zhang, *Chem. Sci.*, 2018, **9**, 3742–3753.
20 Z. Zhang, Y. Zhou, H. Li, T. Gao and P. Yan, *Dalton Trans.*, 2019, **48**, 4026–4034.
21 I. Hernández and W. P. Gillin, in *Handbook on the Physics and Chemistry of Rare Earths*, ed. J.-C. G. Bünzli and V. K. Pecharsky, Elsevier, 2015, ch. 269, vol. 47, pp. 1–100.
22 G. Mancino, A. J. Ferguson, A. Beeby, N. J. Long and T. S. Jones, *J. Am. Chem. Soc.*, 2005, **127**, 524–525.
23 W. Wu, X. Zhang, A. Y. Kornienko, G. A. Kumar, D. Yu, T. J. Emge, R. E. Riman and J. G. Brennan, *Inorg. Chem.*, 2018, **57**, 1912–1918.
24 C. Bischof, J. Wahsner, J. Scholten, S. Trosien and M. Seitz, *J. Am. Chem. Soc.*, 2010, **132**, 14334–14335.
25 C. Doffek, N. Alzakhem, M. Molon and M. Seitz, *Inorg. Chem.*, 2012, **51**, 4539–4545.
26 M. F. K. Trautnitz, C. Doffek and M. Seitz, *ChemPhysChem*, 2019, **20**, 2179–2186.
27 D. Davis, A. J. Carrod, Z. Guo, B. M. Kariuki, Y.-Z. Zhang and Z. Pikramenou, *Inorg. Chem.*, 2019, **58**, 13268–13275.
28 P. B. Glover, A. P. Bassett, P. Nockemann, B. M. Kariuki, R. Van Deun and Z. Pikramenou, *Chem.–Eur. J.*, 2007, **13**, 6308–6320.
29 J.-C. G. Bünzli, A.-S. Chauvin, H. K. Kim, E. Deiters and S. V. Eliseeva, *Coord. Chem. Rev.*, 2010, **254**, 2623–2633.
30 C. Doffek and M. Seitz, *Angew. Chem., Int. Ed.*, 2015, **54**, 9719–9721.
31 S. V. Eliseeva, D. N. Pleshkov, K. A. Lyssenko, L. S. Lepnev, J.-C. G. Bünzli and N. P. Kuzmina, *Inorg. Chem.*, 2011, **50**, 5137–5144.
32 E. R. Trivedi, S. V. Eliseeva, J. Jankolovits, M. M. Olmstead, S. Petoud and V. L. Pecoraro, *J. Am. Chem. Soc.*, 2014, **136**, 1526–1534.
33 J. Jankolovits, C. M. Andolina, J. W. Kampf, K. N. Raymond and V. L. Pecoraro, *Angew. Chem., Int. Ed.*, 2011, **50**, 9660–9664.
34 C. Y. Chow, S. V. Eliseeva, E. R. Trivedi, T. N. Nguyen, J. W. Kampf, S. Petoud and V. L. Pecoraro, *J. Am. Chem. Soc.*, 2016, **138**, 5100–5109.

35 J. C. Lutter, S. V. Eliseeva, J. W. Kampf, S. Petoud and V. L. Pecoraro, *Chem.–Eur. J.*, 2018, **24**, 10773–10783.

36 T. N. Nguyen, C. Y. Chow, S. V. Eliseeva, E. R. Trivedi, J. W. Kampf, I. Martinić, S. Petoud and V. L. Pecoraro, *Chem.–Eur. J.*, 2018, **5**, 1031–1035.

37 I. Martinić, S. V. Eliseeva, T. N. Nguyen, V. L. Pecoraro and S. Petoud, *J. Am. Chem. Soc.*, 2017, **139**, 8388–8391.

38 I. Martinić, S. V. Eliseeva, T. N. Nguyen, F. Foucher, D. Gosset, F. Westall, V. L. Pecoraro and S. Petoud, *Chem. Sci.*, 2017, **8**, 6042–6050.

39 G. Mezei, C. M. Zaleski and V. L. Pecoraro, *Chem. Rev.*, 2007, **107**, 4933–5003.

40 G. Sheldrick, *Acta Crystallogr.*, 2015, **C71**, 3–8.

41 A. Spek, *Acta Crystallogr.*, 2015, **C71**, 9–18.

42 K. K. Innes, I. G. Ross and W. R. Moomaw, *J. Mol. Spectrosc.*, 1988, **132**, 492–544.

43 J.-C. G. Bünzli, *Coord. Chem. Rev.*, 2015, **293–294**, 19–47.

44 W. S. Lo, W. T. Wong and G. L. Law, *RSC Adv.*, 2016, **6**, 74100–74109.

45 Y. Hasegawa, Y. Kitagawa and T. Nakanishi, *NPG Asia Mater.*, 2018, **10**, 52–70.

46 A. D'Aleo, F. Pointillart, L. Ouahab, C. Andraud and O. Maury, *Coord. Chem. Rev.*, 2012, **256**, 1604–1620.

47 W. T. Carnall, P. R. Fields and K. Rajnak, *J. Chem. Phys.*, 1968, **49**, 4443–4446.

48 H. Wei, Z. Zhao, C. Wei, G. Yu, Z. Liu, B. Zhang, J. Bian, Z. Bian and C. Huang, *Adv. Funct. Mater.*, 2016, **26**, 2085–2096.

49 M. Ganapathi, S. V. Eliseeva, N. R. Brooks, D. Soccol, J. Fransaer and K. Binnemans, *J. Mater. Chem.*, 2012, **22**, 5514–5522.

50 A. Beeby, I. M. Clarkson, R. S. Dickins, S. Faulkner, D. Parker, L. Royle, A. S. de Sousa, J. A. G. Williams and M. Woods, *J. Chem. Soc., Perkin Trans. 2*, 1999, 493–503.

51 S. Faulkner, A. Beeby, M.-C. Carrié, A. Dadabhoy, A. M. Kenwright and P. G. Sammes, *Inorg. Chem. Commun.*, 2001, **4**, 187–190.

52 M. H. V. Werts, R. T. F. Jukes and J. W. Verhoeven, *Phys. Chem. Chem. Phys.*, 2002, **4**, 1542–1548.